Dielectric function and plasmon structure of stage-1 intercalated graphite

Kenneth W. -K. Shung
Solid State Division, Oak Ridge National Laboratory, Oak Ridge, Tennessee 37831
and Department of Physics, University of Tennessee, Knoxville, Tennessee 37916
(Received 13 January 1986)

In this paper, we carefully study the dielectric function of stage-1, acceptor-type graphite intercalated compounds (GIC's). We model the system by a superlattice of an infinite number of graphite layers, each of which has the band structure described by the two-dimensional calculation of Blinowski *et al.* Tunneling between graphite layers is neglected, and so are effects due to intercalants except that of determining the Fermi level. However, we have retained a Coulomb term that describes the interaction between electrons on different layers. With this model, we are able to express the result in analytical form, and our treatment is essentially exact. Because of the Coulomb interaction along the c axis, the excitation spectrum has a plasmon band in the (q,ω) plane, where q is the in-plane momentum transfer and ω the energy transfer. This plasmon band is typical for the superlattice structure and contains a three-dimensional mode. We find that, despite the presence of a complicated band structure in GIC's, the three-dimensional characteristics of the plasmons still dominate. A quantitative comparison of plasmon structure between our theory and electron scattering experiments is made in this work. We obtain reasonable agreements between our theory and the measurement, concerning the plasmon energy, the plasmon width, and the plasmon intensity. The agreement suggests that our dielectric function is reliable in describing the dynamic screening mechanism for GIC's.

I. INTRODUCTION

For pure graphite, the conductivity is highly anisotropic: That parallel to the graphite planes is several orders of magnitude higher than that along the c axis. For graphite intercalated compounds (GIC's), the in-plane conductivity is further enhanced. These facts can be understood on the grounds that graphite layers have high in-plane mobility for charge carriers (electrons or holes) and the carrier concentration is increased upon intercalation. As for the conductivity along the c axis, it generally decreases for acceptor-type GIC's—which is the system we shall study in this paper. (For a general review on GIC's, see Ref. 1.) This anisotropic property suggests that the charge transport is mainly two dimensional for GIC's, since the transport along the c axis is negligible compared with the in-plane part. But on the other hand, it was found experimentally[2] that plasmons of GIC's exhibit three-dimensional characteristics; that is, the plasmon energy is finite at small momentum transfer. Therefore, electron correlation between graphite layers is still important, even though the charge tunneling is not. Clearly, a detailed study of electronic properties is necessary in order to understand the somewhat intricate behavior of GIC's.

One major step toward the understanding of electronic properties of GIC's, via microscopic calculation, was made by Blinowski and co-workers,[3] who considered low-stage ($n \leq 4$) GIC's as a set of independent graphite slabs, each containing n graphite layers sandwiched between two layers of intercalants. One should notice that, if the intercalant layers are not present, GIC's become pure graphite and the two-dimensional (2D) model above reverts to the one originally employed by Slonczewski and Weiss[4] for pure graphite. By applying a tight-binding calculation for the graphite part, Blinowski *et al.* obtained the band structure, as well as analytic expressions for the Bloch states, at energies close to the Fermi energy. This result provides us with the basis for a quantitative comparison with the measured optical transitions for acceptor-type GIC's.[3,5] However, this quasi-two-dimensional model of Blinowski *et al.* could not explain the three-dimensional character of the plasmons—understandably, because the graphite slabs are not correlated at all in this model.

In this paper, we would like to extend the model of Blinowski and co-workers so that electron correlations in the c-axis direction can be taken into account. In favor of an analytic final result, and also for the sake of simplicity, we shall only consider the case of stage-1, acceptor-type GIC's. In this system, there is only one graphite layer between two adjacent intercalant layers. We use the results from the calculation of Blinowski *et al.* to describe the electron structure of each such graphite layer. But instead of keeping graphite layers independent of each other, we consider these layers as forming a superlattice with an interlayer distance I_c. We will neglect the interlayer tunneling effects altogether, but will retain the Coulomb-interaction term for electrons in different layers. Therefore, electrons can "feel" the excitations in other layers. The hope is that, by keeping this correlation due to Coulomb interaction, we will be able to appropriately describe the three-dimensional nature of the plasmons.

With the construction of such a superlattice, we will calculate for the system the dielectric function within a self-consistent-field approach.[6,7] Our results are expressed in analytic forms as functions of q (the in-plane momen-

tum transfer) and ω (the energy transfer) and are basically exact according to the wave functions and the band structure of Blinowski *et al.*[3] This dielectric function is then used for examining the plasmon structure by comparing the measurement of Ritsko and Rice.[2] This quantitative comparison shows reasonable agreement between the calculation and the measurement for the plasmon energy, the width, and the strength (as functions of q). Meanwhile, there are some interesting features about plasmons (e.g., a bipeak structure, see Sec. IV), which are direct consequences of a superlattice structure and are not yet observed. Further investigation of these aspects should reveal more about the superlattice structure of GIC's.

Although it has been used mainly for examining the plasmon structure in this work, it should be emphasized that the dielectric function we calculated has prospects of much wider application. This is because dynamic screening effects are very basic to the understanding of systems like GIC's, where the concentration of free charge carriers is high. One demonstration of such an application is given in a separate paper,[8] where we calculated the lifetime of conduction electrons and used it for the interpretation of broadening effects found in optical spectra of GIC's.[3,5]

In the next section, we shall study the model of Blinowski *et al.* for stage-1 GIC's. We will begin by briefly describing their results, and then go on to calculate the dielectric function for the system with only one graphite layer. This calculation is clearly a two-dimensional one, but its results are useful in Sec. III, where we take the c-axis correlation into account by forming a superlattice structure for GIC's. In Sec. IV, we examine the plasmon structure according to our theory, and make quantitative comparison with experimental results. Finally, some concluding remarks are given in Sec. V.

II. 2D MODEL AND $\epsilon^{2D}(q,\omega)$

In this section, we will first summarize the important results from the 2D model of Blinowski *et al.*,[3] and then apply them for the calculation of the dielectric function for a single graphite layer, $\epsilon^{2D}(q,\omega)$. We will use a notation as close as possible to that of Ref. 3, so that easy reference is possible.

In the 2D model for stage-1 GIC's, Blinowski *et al.* calculated the structure of π bands by a simple tight-binding method. In this method, only resonance integrals of nearest neighbors are kept when diagonalizing the Hamiltonian in the subspace spanned by the two tight-binding functions built from atomic $2p$ orbitals, $\phi_z(\mathbf{r})$, of carbon atoms:

$$U_{i\kappa}(r)=C\sum_{\rho_n} e^{i\kappa\cdot(\rho_n+\tau_i)}\phi_z(\mathbf{r}-\rho_n-\tau_i),\quad i=1,2\ . \tag{1}$$

C is the normalization factor and κ is the 2D wave vector. ρ_n is the lattice vector. τ_1 and τ_2 define the positions of atoms in a unit cell; e.g., we can choose

$$\tau_1=0 \text{ and } \tau_2=b\mathbf{e}_x\ ,$$

where $b=1.42$ Å is the nearest-neighbor distance and $\mathbf{e}_x$ the unit vector along the x axis. The energies and wave functions for both valence band and conduction band were found to be (denoted by the superscripts c and v, respectively)

$$\varepsilon_\kappa^{c,v}=\pm\gamma_0|g(\kappa)|\ , \tag{2}$$

$$\psi_\kappa^{c,v}=\frac{1}{\sqrt{2}}\left[U_{1\kappa}\mp\frac{g^*(\kappa)}{|g(\kappa)|}U_{2\kappa}\right]\ . \tag{3}$$

γ_0 is the resonance integral due to the nearest-neighbor interaction and has the value $\gamma_0=2.4$ eV; the function $g(\kappa)$ is defined by

$$g(\kappa)=e^{i\kappa\cdot\tau_2}+e^{i\kappa\cdot D_3\tau_2}+e^{i\kappa\cdot D_3^{-1}\tau_2}\ , \tag{4}$$

where D_3 is the operator of the $2\pi/3$ rotation around the c axis. In the vicinity of either U or U' points (see the Brillouin zone plotted in Fig. 1), where the Fermi level passes through, energy state of Eq. (2) can be simplified by

$$\varepsilon_k^{c,v}=\pm\tfrac{3}{2}\gamma_0 b\,|\mathbf{k}|\equiv\pm v_f k\ . \tag{5}$$

$\mathbf{k}$ is the 2D momentum measured from the U point (or the U' point) and $k=|\mathbf{k}|$. The linear band structure is given in Fig. 1. For pure graphite the Fermi level passes through the degenerate U point. After intercalation (for acceptor-type GIC's), some electrons are transferred from the graphite layer to the intercalant layer, and therefore the Fermi energy is lowered to the level shown in the figure. The Fermi energy ε_F is determined by the relation

$$\varepsilon_F=\gamma_0(\pi\sqrt{3}f/l)^{1/2}\ , \tag{6}$$

where f/l gives the number of holes per carbon atom for the GIC's under consideration.

We are going to use Eqs. (1)–(6) for the evaluation of the $\epsilon^{2D}(q,\omega)$ in the following. To this end, two approximations are applied: (i) We will always use Eq. (5) instead of Eq. (2) for energies. Generally speaking, this approximation is valid as long as the excitation energy is not too

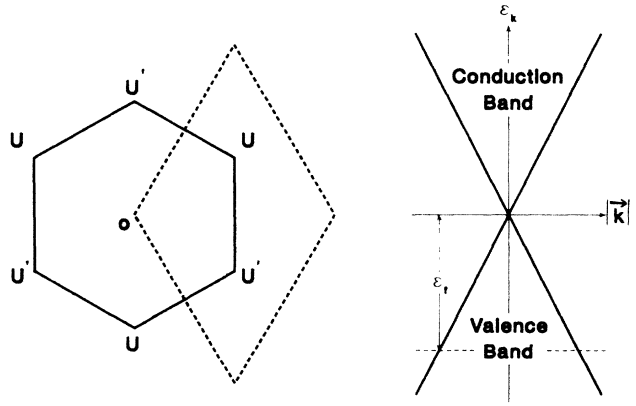

FIG. 1. On the left of this figure is the first Brillouin zone of a graphite layer. Two alternative choices are shown, by the solid and the dashed curves, respectively. The linear band structure found in the vicinity of the symmetric point U (or U') is shown on the right. For acceptor-type GIC's, the Fermi energy is lowered from the degenerate point to a level within the valence band, as indicated in the figure.

large compared with ε_F. More specific arguments concerning the validity of Eq. (5) can be found in Ref. 2. (ii) Concerning ourselves with states in the vicinity of U and U' points, we further regard the two valleys, each around one degenerate point, to be identical and well separated; i.e., we will neglect small effects due to intervalley transitions. This approximation greatly simplifies our formalism and can be easily relaxed.[8]

We can directly apply the result from the self-consistent-field method of Ehrenreich and Cohen,[6] and express the dielectric function in the following form (put $\hbar=1$, here and henceforth):

$$\epsilon^{2D}(q,\omega)=\epsilon_0-4v_q\sum_{\mathbf{k}}\sum_{h=v,c}|\langle\mathbf{k};v\,|\,e^{-i\mathbf{q}\cdot\mathbf{r}}\,|\,\mathbf{k}+\mathbf{q};h\rangle|^2\times\frac{f(\varepsilon^h_{\mathbf{k}+\mathbf{q}})-f(\varepsilon^v_{\mathbf{k}})}{\varepsilon^h_{\mathbf{k}+\mathbf{q}}-\varepsilon^v_{\mathbf{k}}-\omega+i\eta}\,. \tag{7}$$

ϵ_0 is the background dielectric constant contributed from high-energy excitations—other than those excitations within the π bands. Note that the second term now contains both the intraband transitions ($v\to v$) and the interband transitions ($v\to c$). The factor of 4 accounts for the spin degeneracy and the presence of two identical valleys. $f(\epsilon)$ is the usual Fermi distribution function. At $T=0$ K, a state is occupied only if the state lies below the Fermi level. For a single graphite layer, the problem is two-dimensional. Actually, Eq (7) involves an approximation about the Fourier transform of the Coulomb potential, which has the well-known form for 2D systems,

$$v_q(z)=v_q\exp(-q\,|\,z\,|\,),\quad v_q=2\pi e^2/q\,, \tag{8}$$

and $|\,z\,|$ is the distance from the plane. This z-dependent part is neglected here due to the consideration that wave-function extension along the c axis is small (~ 1 Å), while $q\sim 0.1$ Å^{-1} for low-energy excitations, i.e., $\exp(-q\,|\,z\,|\,)=1$. The z dependence of the Coulomb potential will have important effects in the next section where interaction between layers is taken into consideration. Here, for the one-layer system, the calculation of $\epsilon^{2D}(q,\omega)$ comes down to two integrations: one for the calculation of matrix elements $\langle\mathbf{k};v\,|\,e^{-i\mathbf{q}\cdot\mathbf{r}}\,|\,\mathbf{k}+\mathbf{q};v,c\rangle$ and another for summing over all $\mathbf{k}$ states. We will calculate the matrix elements first.

By substituting the wave functions of Eq. (3) for the Bloch states $|\,\mathbf{k};v\rangle$, we find that the matrix elements for intraband excitations have the simple form

$$\langle\mathbf{k};v\,|\,e^{-i\mathbf{q}\cdot\mathbf{r}}\,|\,\mathbf{k}+\mathbf{q};v\rangle=\frac{C^2}{4}\sum_{i=1}^{2}\sum_{\rho_n}\langle\phi_z(\mathbf{r}-\boldsymbol{\rho}_n-\boldsymbol{\tau}_i)\,|\,e^{-i\mathbf{q}\cdot(\mathbf{r}-\boldsymbol{\rho}_n-\boldsymbol{\tau}_i)}\,|\,\phi_z(\mathbf{r}-\boldsymbol{\rho}_n-\boldsymbol{\tau}_i)\rangle\left[1+\frac{g(\mathbf{k}+\mathbf{q})g^*(\mathbf{k})}{|\,g(\mathbf{k}+\mathbf{q})g(\mathbf{k})\,|}\right], \tag{9}$$

where $\phi_z(\mathbf{r})$ is the normalized $2p$ wave function of carbon atoms. In order to get Eq. (9), we have neglected all overlapping integrals between neighboring atoms—an approximation made originally in the 2D model by Blinowski *et al.*[3] The integration of the matrix element can be done analytically if we use a generalized hydrogenic wave function for $\phi_z(\mathbf{r})$,[9] i.e., putting

$$\phi_z(\mathbf{r})=Ar\cos(\theta)e^{-Zr/2a_0}\,. \tag{10}$$

A is a normalization factor, θ is the angle from the c axis, and a_0 is the Bohr radius. Z is an effective core charge chosen to be $Z=3.18$ according to Zener.[9] Note that the wave function in this form has the correct symmetry (for π bands) under reflection about the layer plane. With this hydrogenic wave function, the matrix elements of Eq. (9) can be calculated straightforwardly, and the result is

$$\langle\mathbf{k};v\,|\,e^{-i\mathbf{q}\cdot\mathbf{r}}\,|\,\mathbf{k}+\mathbf{q};v\rangle=\tfrac{1}{2}I(q)\left[1+\frac{g(\mathbf{k}+\mathbf{q})g^*(\mathbf{k})}{|\,g(\mathbf{k}+\mathbf{q})g(\mathbf{k})\,|}\right], \tag{11}$$

where

$$I(q)=\left[1+\left[\frac{qa_0}{Z}\right]^2\right]^{-3}\,. \tag{11a}$$

$I(q)$ is very close to 1 for small q (0.1 Å^{-1}), but becomes much smaller, and hence important, when the momentum transfer is large, e.g., in intervalley transitions. The angle-dependent quantity $g(\mathbf{k})$ was defined earlier by Eq. (4) and could be well approximated[3] in the vicinity of U by

$$g(\mathbf{k})=\tfrac{3}{2}b(b_x-ik_y)\equiv\tfrac{3}{2}bke^{-i\theta_{\mathbf{k}}}\,, \tag{12}$$

where $\theta_{\mathbf{k}}$ defines the direction of the 2D vector $\mathbf{k}$. Since it is the absolute value of these matrix elements that we need for calculating $\epsilon^{2D}(q,\omega)$, we can rewrite Eq. (11) accordingly:

$$|\,\langle\mathbf{k};v\,|\,e^{-i\mathbf{q}\cdot\mathbf{r}}\,|\,\mathbf{k}+\mathbf{q};v\rangle\,|^2=\tfrac{1}{2}I^2(q)\left[1+\frac{k+q\cos(\psi)}{|\,\mathbf{k}+\mathbf{q}\,|}\right], \tag{13}$$

where ψ is the angle between $\mathbf{k}$ and $\mathbf{q}$.

By applying a similar method, we can evaluate the matrix elements for interband transitions. After neglecting the overlapping terms between neighboring atoms and taking the absolute value of the matrix elements, we find

$$|\,\langle\mathbf{k};v\,|\,e^{-i\mathbf{q}\cdot\mathbf{r}}\,|\,\mathbf{k}+\mathbf{q};c\rangle\,|^2=\tfrac{1}{2}I^2(q)\left[1-\frac{k+q\cos(\psi)}{|\,\mathbf{k}+\mathbf{q}\,|}\right], \tag{14}$$

where $I(q)$ and the angle ψ have been defined previously.

We have thus far exactly evaluated the matrix elements of the Coulomb interaction for Bloch states found in the 2D model and expressed the results by Eqs. (11) and (14). Substituting them back into Eq. (7), we can reformulate $\epsilon^{2D}(q,\omega)$ by

$$\epsilon^{2D}(q,\omega)=\epsilon_0-v_q\chi^a(q,\omega)-v_q\chi^b(q,\omega)\ , \tag{15}$$

where

$$\chi^a(q,\omega)=2I^2(q)\sum_{\mathbf{k}}\left[1+\frac{k+q\cos(\psi)}{|\mathbf{k}+\mathbf{q}|}\right]\times\frac{f(\varepsilon^v_{\mathbf{k}+\mathbf{q}})-f(\varepsilon^v_{\mathbf{k}})}{\varepsilon^v_{\mathbf{k}+\mathbf{q}}-\varepsilon^v_{\mathbf{k}}-\omega+i\eta} \tag{15a}$$

defines the response function due to intraband transitions, and

$$\chi^b(q,\omega)=2I^2(q)\sum_{\mathbf{k}}\left[1-\frac{k+q\cos(\psi)}{|\mathbf{k}+\mathbf{q}|}\right]\times\frac{f(\varepsilon^c_{\mathbf{k}+\mathbf{q}})-f(\varepsilon^v_{\mathbf{k}})}{\varepsilon^c_{\mathbf{k}+\mathbf{q}}-\varepsilon^v_{\mathbf{k}}-\omega+i\eta} \tag{15b}$$

defines that due to interband transitions. The evaluation of the response functions is lengthy and is carried out in Appendix A. The imaginary parts of $\chi^a(q,\omega)$ and $\chi^b(q,\omega)$ are calculated exactly. The calculation for the real parts, however, involves expansion for small q and an approximation concerning the band size [i.e., the determination of ϵ_0 in Eq. (A10)]. Details of these approximating procedures can be found in Appendix A. What we would like to emphasize is the following: The region where the approximation is good overlaps with that where the 2D model is applicable; in other words, as long as the 2D model is valid for describing the band structure of GIC's, so is our calculated dielectric function for describing the screening mechanism.

Figure 2 demonstrates the result from our calculation:

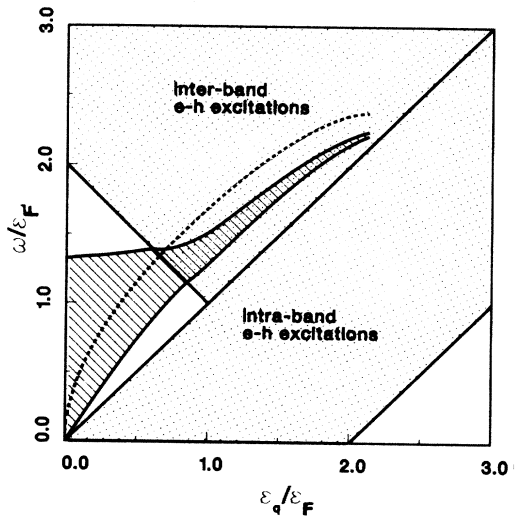

FIG. 2. This is the excitation spectrum calculated from the superlattice model of GIC's. Dotted regions are e-h excitations, as indicated. The cross-hatched region is the plasmon band formed because of the layered structure. The dashed curve is the 2D plasmon curve for a single graphite layer. This spectrum is calculated according to the parameters given in Table I. It should be noted, however, that the spectrum would remain mostly unchanged if other parameters had been used. In that case only the position of the plasmon band needs to be modified.

the excitation energy spectrum as a function of ϵ_q ($\epsilon_q=v_f q$). Because of the special band structure expressed by Eq. (5), intraband excitations are confined to the region where $\omega<\varepsilon_q$, above which both interband excitations and collective-mode excitations (plasmons, shown by the dashed curve) are possible. Excitations corresponding to the cross-hatched region in Fig. 2 are consequences of c-axis correlations and will not be discussed until Sec. III. For a single graphite layer, plasmons are determined by the zeros of $\epsilon^{2D}(q,\omega)$, i.e., by the relation ($\chi=\chi_1+i\chi_2$)

$$\epsilon_0'=\epsilon_0-v_q\chi_1^b(q,\omega)=v_q\chi_1^a(q,\omega)\ . \tag{16}$$

The first equation above defines the background dielectric constant ϵ_0' that includes the contribution from interband transitions. The fact that the part from interband transition is small ($\sim 10^{-2}$) compared with ϵ_0 can be checked easily by directly applying the results from Appendix A. For small q, Eq. (16) leads to a simple dispersion relation for the plasmon energy

$$\omega_p^2(q)=v_q\frac{\varepsilon_f\varepsilon_q^2}{\pi\epsilon_0' v_f^2}+\tfrac{3}{4}\varepsilon_q^2\ , \tag{17}$$

where $v_q=2\pi e^2/q$ from Eq. (8). This result shows that the plasmon energy for a graphite layer indeed has the proper two-dimensional character, i.e., $\omega_p(q)\alpha q^{1/2}$. The plasmon curve in Fig. 2 is determined numerically by solving Eq. (16) without assuming constant contribution from interband excitations, and it agrees closely with Eq. (17). The parameters used in this numerical calculation are the same as those to be used in Sec. IV, where we compare our theory with experiments.

To check our calculation, we examined the f-sum rule[10] which, for a 2D system, has the form [$\epsilon^{2D}(q,\omega)=\epsilon_1^{2D}(q,\omega)+i\epsilon_2^{2D}(q,\omega)$]

$$\int_0^\infty d\omega\,\omega\epsilon_2^{2D}(q,\omega)=\frac{\pi^2e^2n_{2D}q}{m} \tag{18a}$$

for independent-particle excitations, and

$$\int_0^\infty d\omega\,\omega\mathrm{Im}\left[\frac{-1}{\epsilon^{2D}(q,\omega)}\right]=\frac{\pi^2e^2n_{2D}q}{\epsilon_0^2 m} \tag{18b}$$

after screening is taken into account. m is the bare electron mass and n_{2D} is the density of electrons in the π band. The expressions above differ slightly from their three-dimensional (3D) counterparts, mainly because the matrix element of the Coulomb interaction is proportional to q^{-1} now, instead of to q^{-2} in 3D. Note that the f-sum rule is a direct consequence of particle conservation in the system, and therefore Eq. (18) must be exactly satisfied if we have included all possible excitations of π electrons in $\epsilon^{2D}(q,\omega)$. Numerically, the integrals of Eqs. (18a) and (18b) give values that are 60—70 % of the exact ones, for $q<2.5k_f$ in systems of different ϵ_F and ϵ_0. Part of the discrepancy might be explained by the approximations made in our calculation, such as extending the linear band structure ($\varepsilon_k\propto|\mathbf{k}|$) throughout the π bands [see Eq. (A10)], and only including excitations within π bands (i.e., high-energy excitations are neglected). However, these

factors seem too small to explain the large discrepancy found. There are indications that the discrepancy is embedded in the band-structure calculation.[3] We notice that the optical interband transition evaluated by using this band structure [see Ref. 3 and Eq. (33) in the next section], if compared with actual measurements (Refs. 5 and 8), gives the right spectrum profile but is smaller in magnitude by a factor similar to the one we have found above. The nature of this discrepancy is yet to be explained.

In the next section, we will continue our study of GIC's. The assumption made in the 2D model[3] that there is no correlation between layers is relaxed in our treatment. As a result, three-dimensional behavior emerges.

III. THE SUPERLATTICE MODEL OF GIC's

A stage-1 GIC is composed of many evenly spaced graphite layers with one intercalant layer sandwiched between every two adjacent graphite layers. As noted in the Introduction, electron transport between layers is not important for the system. Nevertheless, excitations in one layer can affect electrons on other layers via the Coulomb potential, see Eq. (8). Therefore, it is important to properly take into account both the three-dimensional lattice structure and the Coulomb interaction when modeling the system. One natural extension in this direction from the 2D model of GIC's is to construct a superlattice. This superlattice is composed of infinite identical graphite layers (hence surface effects are neglected) and each has the band structure described by the 2D model, i.e., by Eqs. (1)—(6). Effects of intercalants are restricted to the determination of ϵ_F by Eq. (6) and are otherwise neglected. Because of low charge-particle mobility in the z direction, we neglect the interlayer tunneling altogether. The Coulomb interaction for electrons on different layer is certainly retained, since this is the very reason why we construct a superlattice for GIC's. As will be shown below, one can easily calculate the dielectric function for this superlattice system and express the function in terms of $\chi^{a,b}(q,\omega)$ of Eq. (15). Using the dielectric function, we then proceed to examine the dimensionality of plasmons for this superlattice system. The results will be compared with experiments later in Sec. IV.

The superlattice model of GIC's introduced above is very similar in structure to the one composed of infinite layers of 2D electron gas (2DEG). The latter has been extensively studied[7,11] and the results from these treatments can be applied to our system with only minor modification. The necessary modification arises from the difference in band structure of the two systems. For the graphite layers, there are both the valence band and the conduction band; hence the q-component electron-density operator has the form

$$\hat{\rho}(q)=\sum_l \hat{\rho}_l(q)=\sum_l \sum_{\mathbf{k}} \sum_{h_1,h_2=v,c} |\mathbf{k}+\mathbf{q};h_1\rangle\langle \mathbf{k}+\mathbf{q};h_1|e^{i\mathbf{q}\cdot\mathbf{r}}|\mathbf{k};h_2\rangle\langle \mathbf{k};h_2| \ , \tag{19}$$

where l is the layer index and q is the two-dimensional momentum transfer. It is important to keep the matrix element

$$\langle \mathbf{k}+\mathbf{q};h_1|e^{i\mathbf{q}\cdot\mathbf{r}}|\mathbf{k};h_2\rangle$$

in the expression, since its value differs from 1, as has been demonstrated in the calculation of Eqs. (11) and (12). Another problem concerning the z-direction extension of the Bloch states $|\mathbf{k};v,c\rangle$ on the other hand—see Eqs. (1), (3), and (10)—can be solved easily. This is because the extension is small compared with other length scales in the system, e.g., I_c and q^{-1} [see the argument following Eq. (8)]. Thus we can apply Eq. (8) and put the z-component Coulomb interaction between layers l_1 and l_2 by

$$V_{l_1,l_2}(q)=V_l(q)|_{l=l_1-l_2}=v_q\exp(-q\,|\,l\,|\,I_c) \ . \tag{20}$$

With this approximation, we have erased the problem regarding the thickness of graphite layers. The remaining difficulty due to the band structure of GIC's is simplified by the assumptions generally made for superlattices that interlayer tunneling is neglected and that layers are identical to each other.[7,11] One important consequence of these assumptions is that the dielectric function of a superlattice can be constructed by the response functions that describe the 2D system, and hence only depends indirectly on the band structure of each layer. In other words, we can apply the results of Refs. 7 and 11 for GIC's by merely substituting the response functions contained therein, using instead those of a graphite layer, which we have evaluated in Sec. II. To demonstrate this relation, we outline below the derivation of a dielectric function for GIC's which has the charge density defined by Eq. (19). Detailed derivation parallels that of Refs. 7 or 11.

Let us suppose that there is an external charge with the frequency ω interacting with the system. The time-dependent potential from this external charge perturbs electrons on the layer l with the strength

$$\hat{v}_l^{\,\mathrm{ex}}(q,\omega)=\frac{1}{\epsilon_0}v_l^{\mathrm{ex}}(q,\omega)\hat{\rho}_l(q)e^{-i\omega t} \ , \tag{21}$$

where the operator $\hat{\rho}_l(q)$ is defined by Eq. (19) and ϵ_0 is the background screening constant. There is no cross term for different layers because interlayer tunneling is neglected. This external field can induce charge fluctuation of magnitude $\rho_l^{\mathrm{in}}(q,\omega)$, which, in turn, builds up its own field $v_l^{\mathrm{in}}(q,\omega)$. Effectively, electrons on the layer l are affected by a screened perturbing potential that is the combination of the two, i.e.,

$$\begin{aligned}\hat{v}_l^{\,\mathrm{eff}}(q,\omega)&=\hat{v}_l^{\,\mathrm{ex}}(q,\omega)+\hat{v}_l^{\,\mathrm{in}}(q,\omega)\\&\equiv v_l^{\mathrm{eff}}(q,\omega)\hat{\rho}_l(q)e^{-i\omega t} \ .\end{aligned} \tag{22}$$

A standard calculation of the linear response to the effective potential gives the relation[6,10]

$$\rho_l^{\mathrm{in}}(q,\omega)=v_l^{\mathrm{eff}}(q,\omega)[\chi^a(q,\omega)+\chi^b(q,\omega)] \ , \tag{23}$$

where $\chi^{a,b}(q,\omega)$ are the response functions of a graphite layer and are defined by Eq. (15). It should be noted that the response functions do not depend on the index l since all layers are identical to each other. In order to get Eq. (23), we have applied the so-called random-phase approximation (RPA), by which we can neglect interaction between particles after we have determined the effective potential. This effective potential ought to be self-consistently determined from Eqs. (22) and (23), together with a third equation that relates the induced charge and the induced potential:

$$\hat{v}_l^{\text{in}}(q,\omega)=\sum_{l'}\frac{1}{\epsilon_0}V_{l-l'}(q)\rho_{l'}^{\text{in}}(q,\omega)\hat{\rho}_l(q)e^{-i\omega t}\ . \tag{24}$$

This last equation states the simple fact that the induced potential occurring on layer l is contributed by all induced charges, including those on other layers. By substituting Eqs. (23) and (24) back into Eq. (22), we find

$$\epsilon_0 v_l^{\text{eff}}(q,\omega)=v_l^{\text{ex}}(q,\omega)+\sum_{l'}V_{l-l'}(q)v_{l'}^{\text{eff}}(q,\omega)\times[\chi^a(q,\omega)+\chi^b(q,\omega)]\ , \tag{25}$$

which is the self-consistent relation we are looking for. One simple application of this result is for a single graphite layer. In that case the summation over l' contains only one term ($l=l'=0$). With the definition that the dielectric function is the ratio between the external potential and the effective potential, we readily recover $\epsilon^{2D}(q,\omega)$ of Eq. (15).

For a superlattice that has infinite graphite layers, it is more convenient to apply Eq. (25) in its Fourier-transformed expression. Due to the periodic structure of the superlattice, we can define

$$\sum_l v_l^{\text{ex}}(q,\omega)e^{ik_z lI_c}=v^{\text{ex}}(q,k_z,\omega)$$

and (26)

$$\sum_l v_l^{\text{eff}}(q,\omega)e^{ik_z lI_c}=v^{\text{eff}}(q,k_z,\omega)\ ,$$

where k_z is confined to the first Brillouin zone, i.e., $|k_z|<\pi/I_c$. We can rewrite Eq. (25) accordingly ($v_q=2\pi e^2/q$),

$$\epsilon_0 v^{\text{eff}}(q,k_z,\omega)=v^{\text{ex}}(q,k_z,\omega)+v^{\text{eff}}(q,k_z,\omega)v_q S(q,k_z)\times[\chi^a(q,\omega)+\chi^b(q,\omega)]\ , \tag{27}$$

where

$$S(q,k_z)=\frac{1}{v_q}\sum_l V_l(q)e^{ik_z lI_c}=\frac{\sinh(qI_c)}{\cosh(qI_c)-\cos(k_z I_c)}\ . \tag{28}$$

Defining the dielectric function as usual, we finally get[7,11]

$$\epsilon(q,k_z,\omega)=\frac{v^{\text{ex}}(q,k_z,\omega)}{v^{\text{eff}}(q,k_z,\omega)}=\epsilon_0-v_q S(q,k_z)[\chi^a(q,\omega)+\chi^b(q,\omega)]\ . \tag{29}$$

As we have expected, $\epsilon(q,k_z,\omega)$ is indeed constructed from the 2D response functions. In fact, $\epsilon(q,k_z,\omega)$ differs from $\epsilon^{2D}(q,\omega)$ merely by an extra structure factor $S(q,k_z)$ that describes the layered structure. It should be noted that k_z has nothing to do with z-direction momentum transfer, since there is no interlayer tunneling allowed in our formalism. The actual meaning of k_z is contained in Eq. (26). In the following, we are going to discuss the property of $\epsilon(q,k_z,\omega)$.

It is obvious from Eq. (29) that the spectrum of electron-hole excitations overlaps with that of a graphite layer in the q,ω space, as is shown in Fig. 2. On the other hand, the plasmon spectrum of a superlattice is very different from its 2D counterpart. It forms a band in the q,ω space, as is also shown in Fig. 2. The presence of this plasmon band can be understood by the fact that, for a given q, each k_z determines one particular plasmon energy. We found that the plasmon energy increases as k_z decreases, and that the high-energy edge of the plasmon band corresponds to $k_z=0$ and the low-energy edge to $k_z=\pi/I_c$. At the above two limits, the structure factor has the following value for small q:

$$S(q,k_z)\approx\begin{cases}\dfrac{2}{qI_c}, & \text{if } k_z=0,\ \text{as } q\to 0\\ \dfrac{qI_c}{2}, & \text{if } k_z=\dfrac{\pi}{I_c},\ \text{as } q\to 0\ .\end{cases} \tag{30}$$

Considering the similarity between $\epsilon(q,k_z,\omega)$ and $\epsilon^{2D}(q,\omega)$, it is easy to infer from Eq. (17) that the k_z-dependent plasmon energy of the superlattice system is (for small q)

$$\omega_p^2(q,k_z)=v_q S(q,k_z)\frac{\varepsilon_F\varepsilon_q^2}{\pi\epsilon_0' v_f^2}+\tfrac{3}{4}\varepsilon_q^2\ . \tag{31}$$

Therefore, the upper edge of the plasmon band behaves as do 3D plasmons; i.e., we can approximate the plasmon energy by the expression

$$\omega_p(q,k_z=0)\approx\omega_p^0+\alpha q^2\ , \tag{32a}$$

where

$$\omega_p^0=\left[\frac{4e^2\varepsilon_F}{\epsilon_0' I_c}\right]^{1/2}\quad\text{and}\quad\alpha=\frac{3}{8}\frac{v_f^2}{\omega_p^0}\ .$$

As for the lower edge, the plasmon energy is linear in q:

$$\omega_p(q,k_z=\pi/I_c)\sim\alpha' q\ , \tag{32b}$$

where

$$\alpha'=\left[\frac{e^2 I_c\varepsilon_F}{\epsilon_0'}+\tfrac{3}{4}v_f^2\right]^{1/2}\ .$$

The expressions above need some explanation concerning ϵ_0', which, as a matter of fact, is not a constant. As was defined in Eq. (16) for a graphite layer, ϵ_0' is the background screening factor that includes the contribution from interband excitations. Note that the latter now varies strongly for different k_z since $S(q,k_z)$ does also;

e.g., see Eq. (30). Thus one needs to numerically determine ϵ_0' as a function of q, k_z, and ω in actual calculations. The calculation of the excitation spectrum of Fig. 2, as well as all other calculations, is done in this way. A specific example of determining ϵ_0' can be found in Sec. IV.

Before going on with our investigation of plasmons of GIC's, it is interesting to compare our results with those of Blinowski *et al.*,[3] since we have applied the band structure from their calculation. We note that the plasmon energy ω_p^0 found in Eq. (32a) agrees with the value derived by them[3] from a different approach [see Eq. (20) therein]. The difference is that they used the 3D Coulomb potential $(4\pi e^2/q^2)$ from the very beginning, and therefore they only found one plasmon energy at $q=0$. Another interesting comparison between the two theories is for interband transitions at $q=0$, corresponding to optical transitions. It is easy to show, by using Eq. (A11), that

$$\lim_{q\to 0}\lim_{k_z\to 0}[-v_q S(q,k_z)\chi_2^b(q,\omega)]=\frac{\pi e^2}{I_c\omega}\Theta(\omega-2\varepsilon_F)\ , \tag{33}$$

and this is exactly the optical transition spectrum found in Ref. 3, see Eq. (27) and put $T=0$ K therein. This agreement is expected, since longitudinal dielectric functions should reduce to transverse ones in the long-wavelength limit ($q=0$).[10] What one might like to know is whether or not it is valid for us to explain the optical transition by using one particular mode [$k_z=0$ in Eq. (33)] out of many possible choices, or, equivalently, for Blinoski *et al.*[3] to directly use the 3D Coulomb potential to start with. In order to answer this question more study is needed, and we do not make such an attempt in this work.

We could gain some knowledge about the plasmon properties from examining the plasmon strength as a function of q and k_z. For this purpose, let us define a quantity $\beta(q,k_z,\omega)$ by the following relation:

$$\mathrm{Im}\left[\frac{-S(q,k_z)}{\epsilon(q,k_z,\omega)}\right]=\beta(q,k_z',\omega)\delta(k_z-k_z')\ , \tag{34a}$$

where k_z' satisfies $\omega=\omega_p(q,k_z')$, or equivalently,

$$\beta(q,k_z,\omega)=\pi S(q,k_z)\left|\frac{\partial\epsilon_1(q,k_z,\omega)}{\partial k_z}\right|^{-1}_{\omega=\omega_p(q,k_z)}$$
$$=\frac{\pi\sinh(qI_c)}{\epsilon_0'\sin(k_zI_c)}\ . \tag{34b}$$

The last equation above follows directly from the definition of $\epsilon(q,k_z,\omega)$. One readily finds that $\beta(q,k_z,\omega)$ is singular on both edges of the plasmon band (where $k_zI_c=0$ and π, respectively) and forms a deep valley between the two edges, see also Figs. 4 and 5 in Sec. IV. A quantity that measures the total plasmon strength at given q is calculated:

$$\beta(q)=\int_{\omega_p(q,k_z=\pi/I_c)}^{\omega_p(q,k_z=0)}\beta(q,k_z,\omega)d\omega\ . \tag{35}$$

The ratio $\beta(q)/\beta(0)$ is plotted in Fig. 3, which shows $\beta(q)$ to be nearly constant for $q=0$ up to q_c, the critical momentum transfer at which plasmons begin to decay into interband electron-hole pairs [i.e., where $\chi_2^b(q,\omega)\neq 0$]. The distribution of the plasmon strength for given q is also of interest. Let us divide the plasmon band into the high-energy region (H) and the low-energy region (L) and study the relative strength of the two. We choose the dividing point of the two regions to be at $k_zI_c=\pi/2$, which is the minimum of $\beta(q,k_z,\omega)$. Plasmon strength in both regions is calculated:

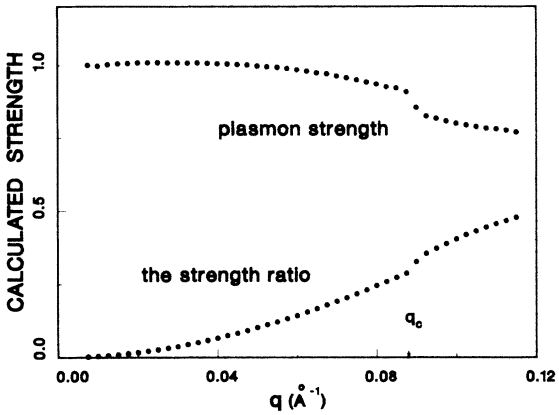

FIG. 3. The calculation of $\beta(q)$ [to be weighted by $\beta(0)$] shows that the plasmon strength is consistent for $q<q_c$ (q_c is the critical momentum, beyond which plasmons are damped). Also shown is the plasmon ratio $\beta^L(q)/\beta^H(q)$, see Eq. (36). This ratio demonstrates that the $k_z=0$ plasmon modes, and hence the 3D characteristics, prevail at small q.

$$\beta^L(q)=\int_{\omega_p(q,k_z=\pi/I_c)}^{\omega_p(q,k_z=\pi/2I_c)}\beta(q,k_z,\omega)d\omega\ ,$$

$$\beta^H(q)=\int_{\omega_p(q,k_z=\pi/2I_c)}^{\omega_p(q,k_z=0)}\beta(q,k_z,\omega)d\omega\ . \tag{36}$$

The ratio $\beta^L(q)/\beta^H(q)$, also shown in Fig. 3, demonstrates an important result. We notice that for small q, $\beta^H(q)$ is the dominating part and $\beta^L(q)$ is negligible. Since high-energy plasmons exhibit 3D character, as was shown by Eq. (32a), we can conclude that for small q, plasmons of GIC's are basically three dimensional in character—a fact found experimentally.[2,5] This rather conclusive statement ought to be checked with experimental results on a quantitative basis, and that will be done in the next section. There, we examine the plasmon structure from electron scattering experiments.[2] In a separate paper,[8] we have applied our theory to explain the edge structure in optical interband transitions.[5]

IV. THE PLASMON STRUCTURE OF GIC'S

In this section, we proceed to compare the plasmon structure between our theory and the measurement by Ritsko and Rice.[2] We note that measured plasmon dispersion has been studied by Mele and Ritsko based on a modified superlattice model.[12] Compared with that work, the present theory has more extended scope and also pro-

vides more details. Experimentally, one measures the energy-loss spectrum as a function of the 2D momentum transfer q. From the spectrum, one can then determine the plasmon energy, the plasmon width, and the plasmon intensity. To second-order (Born) approximation, the electron-loss spectrum can be theoretically formulated in terms of the dielectric function,[10] which we have evaluated for GIC's in the preceding sections. Therefore, a close comparison between our theory and the measurement is possible. In the process, however, we need to be careful in determining the external potential $v_l^{ex}(q,\omega)$, as is discussed below.

In the problem, we want to evaluate the electron energy loss due to electronic excitations in GIC's. These excitations are created because electrons on a layer (denoted by l) are perturbed by a potential $v_l^{eff}(q,\omega)$—the screened potential arising from the probing electron. According to the Fermi golden rule, the probability per unit time $P(q,\omega)$ that the probing electron transfers momentum q and energy ω to electrons in a GIC sample is given by

$$P(q,\omega)=2\sum_l [v_l^{eff}(q,\omega)]^2 \mathrm{Im}[\chi^a(q,\omega)+\chi^b(q,\omega)] , \quad (37a)$$

where we have applied the definition of $\chi^{a,b}(q,\omega)$, Eq. (15). By using Parseval's theorem, we can express $P(q,\omega)$ in k_z space where the linear screening relation, i.e., Eq. (29), is applicable; thus we get

$$P(q,\omega)=\frac{I_c}{\pi}\int_{-\pi/I_c}^{\pi/I_c} dk_z \left|\frac{v^{ex}(q,k_z,\omega)}{\epsilon(q,k_z,\omega)}\right|^2 \times \mathrm{Im}[\chi^a(q,\omega)+\chi^b(q,\omega)] . \quad (37b)$$

This last expression is very similar to the result for a 3DEG, where $P(q,\omega)$ is proportional to the dynamic form factor.[10] In the case of layered systems like GIC's, we need to appropriately determine $v^{ex}(q,k_z,\omega)$ and afterwards do the integration. For this purpose, we will consider two limiting cases below: in one case the probing electron has well-defined momentum, in the other case it has well-defined position.

A state with well-defined momentum is represented by a plane wave, which has a uniform density in space. This means the potential $v_l^{ex}(q,\omega)$ is independent of l, and hence only the $k_z=0$ mode is activated [see Eq. (26)]. From Eq. (30) and the argument that follows, we can conclude that the plasmon detected is strictly three dimensional. This result agrees with the finding of 3D plasmons, but the validity of the assumption that the external particle in the experiment is uniformly distributed in space is arguable, since GIC's have large interlayer distance ($I_c=9.42$ Å). In the measurement,[2] the 2D momentum transfer has a resolution of 0.055 Å^{-1}. Suppose the momentum uncertainty along the c axis has a comparable magnitude; we would then expect the probing electron to be better described by a wave packet of size $\sim I_c$. In our treatment below, we would approximate this case by a zero-width wave packet located on the layer $l_0=0$. We choose to work with this limiting case for the following reasons: (i) It turns out to be a good approximation for a finite-size wave packet (see Appendix B), (ii) an analytical result for the energy-loss spectrum is possible for both plasmons and electron-hole excitations (see Appendix B also), (iii) this is a case in which all the modes in the plasmon band can be excited and it is interesting to examine the plasmon behavior in this instance, and lastly (iv) the formalism so obtained is useful in dealing with dynamic screening effects for processes that are taking place on graphite layers, for example, in the calculation of a conduction electron's lifetime.[8]

With this approximation, then, the electronic excitations are due to a narrow wave packet at the layer l_0. The unscreened potential on the layer l, $v_l^{ex}(q,\omega)$, is simply $V_l(q)$ according to Eq. (20). From Eqs. (26) and (28), we immediately get $v^{ex}(q,k_z,\omega)=v_q S(q,k_z)$. Thus, $P(q,\omega)$ can be reformulated:

$$P(q,\omega)=2v_q\frac{I_c}{2\pi}\int_{-\pi/I_c}^{\pi/I_c} dk_z S(q,k_z)\mathrm{Im}\left[\frac{-1}{\epsilon(q,k_z,\omega)}\right] \equiv 2\pi(v_q)^2 D^s(q,\omega)\equiv 2v_q \mathrm{Im}\left[\frac{-1}{\epsilon^s(q,\omega)}\right] . \quad (38)$$

This last equation defines $D^s(q,\omega)$ and also, for notational convenience, a dimensionless quantity $\mathrm{Im}[-1/\epsilon^s(q,\omega)]$, where the superscript s indicates the superlattice structure. Note that $D^s(q,\omega)$ can be interpreted to be the dynamic form factor of the superlattice system. $D^s(q,\omega)$, or $\mathrm{Im}[-1/\epsilon^s(q,\omega)]$, can be analytically calculated. Actually, we have already done this for plasmons; from Eq. (34), we get

$$\mathrm{Im}[-1/\epsilon^s(q,\omega)]=\beta(q,k_z,\omega) . \quad (39)$$

The calculation of $D^s(q,\omega)$ for electron-hole excitations is straightforward but lengthy, and is detailed in Appendix B.

Before we can calculate $P(q,\omega)$ and make comparison with experiments, we need to determine two parameters, namely, the Fermi energy ε_F and the background screening factor ϵ_0'. These two quantities are related to each other through the plasmon energy ω_p^0, Eq. (32a). Hence, all three need to be determined consistently. We are most certain about ω_p^0 from Ref. 2, which puts $\omega_p^0=1$ eV. The Fermi energy is not accurately known and lies between 0.5 and 1.0 eV. We take its mean value at 0.75 eV, which corresponds to a charge transfer per carbon atom $f/l=0.018$, according to Eq. (16). For a reference, we note that Mele and Ritsko[12] put $f/l=0.015$ and found their best agreement with the measurement. Having determined ω_p^0 and ε_F, we find $\epsilon_0'=4.58$ from Eq. (32a). As noted in Sec. III, ϵ_0' varies according to q, k_z, and ω. The chosen value of ϵ_0' is thus only valid at the plasmon mode ω^0. (The corresponding dielectric constant in Ref. 12 is 5.) By definition, ϵ_0' contains the part due to inter-π-band transitions, cf. Eq. (16); i.e.,

$$\epsilon_0'=\epsilon_0-v_q S(q,k_z)\chi_1^b(q,\omega) \quad (40a)$$

$$=\epsilon_0-\frac{e^2}{I_c}\left[\frac{1}{\omega}\ln\left|\frac{2\varepsilon_F-\omega}{2\varepsilon_F+\omega}\right|+\frac{1}{\varepsilon_D}\right]_{\omega=\omega_p^0}, \quad \text{if } q\to 0 \text{ and } k_z=0 , \quad (40b)$$

TABLE I. Parameters used in our calculation.

Lattice parameters			Electronic parameters		
b[a] (Å)	γ_0[a] (eV)	I_c[b] (Å)	ε_F[c] (eV)	ω_p^0[c] (eV)	ϵ_0[d]
1.42	2.4	9.42	0.75	1	2.4

[a]Reference 3.
[b]Reference 5, also $I_c=9.4$ from Ref. 2.
[c]Reference 2.
[d]This work.

which follows directly from Eqs. (A12') and (A13). ε_D is a measure of the band size and is defined and evaluated in Eq. (A10). This result means that ϵ_0, the screening constant due to all excitations outside of π bands, is 2.4. It is interesting to note that Taft and Philipp found,[13] for pure graphite, the same screening constant due to high-energy excitations. Whether or not this close agreement implies anything of significance is not clear at the moment.

Now we have obtained all the parameters necessary for our calculation. These parameters are summarized in Table I. We would like to emphasize that all these parameters are not "adjustable" in our theory; however, the determination of ε_F, ω_p^0, and ϵ_0 depends heavily on accurate measurements.

Let us examine the spectra shape first. We calculate $\mathrm{Im}[-1/\epsilon^s(q,\omega)]$ as functions of ω at selected q, and plot the result on the left of Fig. 4. The calculation is restricted to the region $\omega<3$ eV, where our theory is valid. We choose to calculate $\mathrm{Im}[-1/\epsilon^s(q,\omega)]$ because we can demonstrate the spectra more clearly this way, and yet can easily convert it to $P(q,\omega)$ by multiplying it by a factor $\propto(1/q)$. A very distinctive bipeak structure is found for the $(q=0.1)$-Å^{-1} curve, obviously due to the two plasmon modes at $k_z=0$ and π/I_c. At higher q (0.21 and 0.28 Å^{-1}), the bipeak structure disappears and the plasmon becomes a broad peak in shape. The disappearance of the bipeak structure is due to two effects: first, the plasmon band becomes narrower at larger q; and second, damping due to interband transitions becomes active (see Fig. 2 and note that $\varepsilon_q=0.51$ eV for $q=0.1$ Å^{-1}). At still higher q (0.35 Å^{-1}), one can no longer find a well-defined plasmon structure—understandably, because the damping is too strong now. Measured spectra at the corresponding momentum transfers can be found in Fig. 1 of Ref. 2. Before we can actually compare the spectra, we need to include in our calculation the broadening effects that are inherent in the measurement. Ritsko and Rice reported an energy resolution of 0.11 eV full width at half maximum (FWHM) and a momentum resolution of 0.055 Å^{-1} FWHM. Taking into account these broadening effects by convoluting our spectrum with a pair of Gaussians of the reported FWHM, we get the broadened spectra which are shown on the right of Fig. 4. All theoretical curves are now in good agreement with the measured spectra, especially for the plasmon peaks [remembering that the calculated curves should be multiplied by a factor $\propto(1/q)$ before comparing, see Eq. (38)]. Note that the bipeak plasmon structure found previously has disappeared by now, because of the broadening.

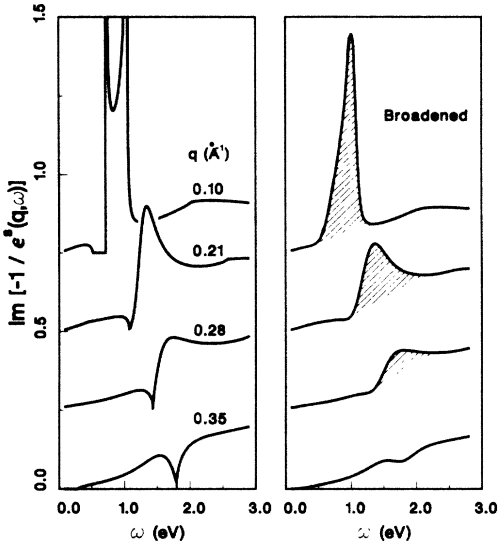

FIG. 4. We plot on the left of this figure the unbroadened energy-loss spectra at selected momentum transfers. Note that $\mathrm{Im}[-1/\epsilon^s(q,\omega)]$ is a dimensionless quantity, and that a constant weight (0.25) has been added to each successive spectrum to separate the curves. After we include the broadening, the spectra are modified, as shown on the right. The most drastic change due to broadening is that the bipeak plasmon structure of the $q=0.1$ Å^{-1} spectrum becomes a single-peak one. The shaded peaks show the plasmon structure and are used later on for direct comparison with measurements.

The disappearance of the bipeak structure due to broadening was further studied. Two facts about the plasmon band are important to this effect: (i) the lower-energy plasmon peak is weaker in strength, see Fig. 3, and (ii) the energy of $k_z=\pi/I_c$ plasmons strongly depends on q but that of $k_z=0$ plasmons does not, see Fig. 3 and Eqs. (32a) and (32b). It is due to the second fact that the weaker plasmon peak becomes smeared out when broadening in q is taken into account; this is because we are then sampling the $k_z=\pi/I_c$ plasmons at very different energies. In order to observe the bipeak plasmon structure predicted by our theory, we ought to look at a region where the $k_z=\pi/I_c$ plasmons are not too weak (this means that q should not be too small) while the damping is not too strong (q not too large), and most importantly, we must keep the momentum resolution high. Figure 5 shows our calculated spectrum for $q=0.11$ Å^{-1} at different momentum resolutions. The dashed curve is the unbroadened spectrum, which shows two strong plasmon peaks (note that the $k_z=0$ plasmon is slightly damped but the $k_z=\pi/I_c$ is not). The $n=1$ curve has been broadened as before and shows no trace of a second peak. We double the momentum resolution (reducing FWHM by half) each time for the subsequent three curves. A broad shoulder is observed to develop at the low-energy side of the 3D plasmon peak. And finally, in curve 4, the weak second peak appears. According to this calculation, we need to improve the momentum resolution at least by a factor of 10 in order to experimentally observe the bipeak plasmon structure of GIC's.

After broadening is applied, plasmons are determined to be the shaded peaks in Fig. 4. This procedure of mapping out the plasmon structure is similar to what is done experimentally.[2] With these plasmon peaks, we can easily determine the position, the width, and the intensity of the plasmons, and can directly compare our results with the measurements.

First, we compare the plasmon energies, shown by Fig. 6. The straight line, as a reference, is plotted according to Eq. (32a), i.e., the small-q approximation for $k_z=0$ plasmons. The slope of this curve is $\alpha=1.28m$ (m is the electron mass), which is close to the measured value[2] ($1.62m$). In fact, if the two experimental data points (solid squares) at large q were discarded, the agreement would be much closer. The calculated peak positions are shown by solid circles; the curve which they define has a slope which is well described by the small-q approximation, although the plasmon energies are somewhat lower at all q. Also plotted in this figure are the actual energies of the $k_z=0$ plasmons (crosses). It is seen that, for $q^2>0.02$ Å^{-2}, broadening does not affect the plasmon energy very much. At smaller q, however, broadening causes the plasmon energy to red shift, and this is because the plasmon band there is wide and extends one-sidedly to the lower-energy region from the $k_z=0$ modes (see Fig. 2). Two points could be drawn from our argument above: first, that our theory satisfactorily explains the quadratic dispersion relation of the plasmon energy, and second, that due to broadening effects, measured plasmon energy at $q=0$ would be red shifted from ω_p^0 (i.e., the system

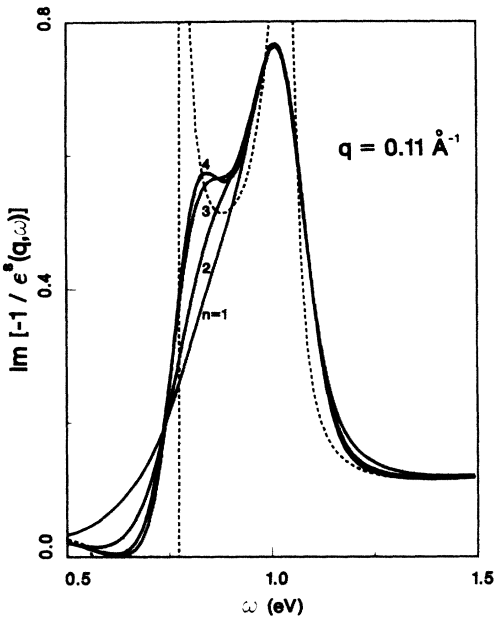

FIG. 5. We examine the broadening effects on the plasmon structure in this figure. The dashed curve is the unbroadened spectrum which shows a very distinctive bipeak structure. The four solid curves are broadened, respectively, by a Gaussian in q of 0.055 Å$^{-1}/(2)^{n-1}$ FWHM, as well as one in ω (0.11 eV FWHM). One can clearly see that, as the resolution improves, the weaker peak becomes more and more visible and becomes well-defined in the curve $n=4$.

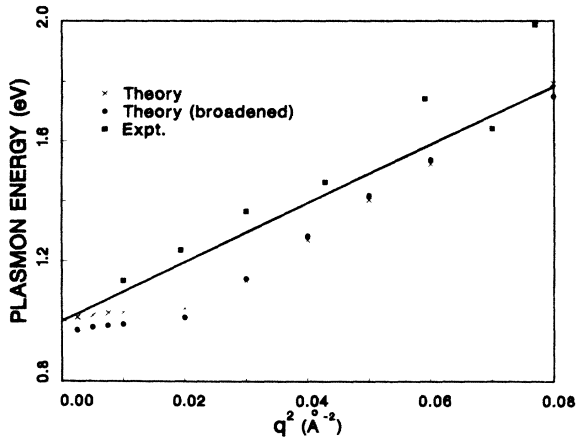

FIG. 6. Experimentally measured plasmon energies are shown by the solid squares, which should be compared with our calculated results denoted by the solid circles. Also shown are the plasmon energies of $k_z=0$ modes denoted by crosses. The small-q approximation from the $k_z=0$ modes is shown by the straight line. It should be noted that the slope of this line agrees with that of either the measured results or the calculated ones.

Ritsko and Rice used for measurement probably has ω_p^0 higher than 1 eV).

Calculated plasmon widths (solid circles) and the measured widths (solid squares) are plotted in Fig. 7. There is a difference in FWHM of about 0.04 eV, which in the present theory could not be accounted for. The difference is probably due to the fact that our theory does not include all possible decay channels for plasmons, e.g., phonons, multi-electron-hole-pair excitations, etc. Besides this small difference, however, the agreement is very good, especially for the overall shape. In the small-q re-

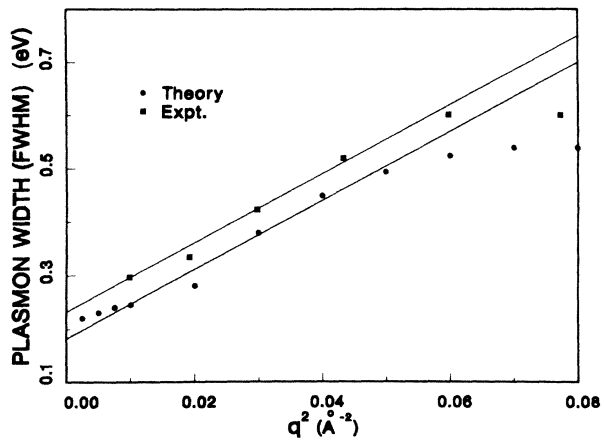

FIG. 7. Measured and calculated plasmon widths are plotted in this figure. Despite a slight difference in magnitude ($\sim$0.03 eV), the two results agree well with each other. The two lines shown are fitted to the data points in order to demonstrate the quadratic q dependence at small q. The slope of the lines is 6.4 eV Å^{-2}.

gion, both the calculated and the measured widths could be approximated by a relation quadratic in q, with a slope of 6.4 eV Å^{-2} (the straight lines).

The plasmon intensity is measured by both the peak height (solid squares) and the peak area (open squares). Correspondingly, we have calculated the peak height (solid circles) and the peak area (open circles) and show the results in Fig. 8. The intensity is normalized about the value at $q=0.1$ Å^{-1} and plotted logarithmically as a function of q. There are no reported experimental data for $q<0.1$ Å^{-1}, so only the theoretical results are given there. In the region where comparison is possible, we find a large discrepancy: the calculated intensity is larger than the measured one by a factor of 2—4. Actual causes for this disagreement are not known. In our opinion, it would be difficult to tell whether or not there is a real disagreement with our theory before accurate measurements for $q<0.1$ Å^{-1} are available. This is because the q dependence at small q is very different from that at large q, according to our theory. In fact, we find that the q dependence varies constantly as q changes (see Fig. 8): the plasmon intensity falls $\propto q^{-1}$ for $q<0.1$ Å^{-1} where plasmons are undamped; it falls off faster and faster as q increases, due to damping effects, and becomes proportional to $q^{-3.5}$ for $q>0.15$ Å^{-1}. Experimentally, the reported peak height follows the q^{-4} pattern in the whole region where the measurement is taken (0.1 Å$^{-1}<q<0.25$ Å^{-1}). This result, according to our theory, suggests that plasmons at $q=0.1$ Å^{-1} are already heavily damped. One possible explanation for this is, for example, that the actual Fermi energy is smaller than 0.75 eV—the value we used in our calculation. In other words, we need the accurate ε_F, as well as ω_p^0 and ϵ_0, for our calculation so that the results can be closely compared with experiments.

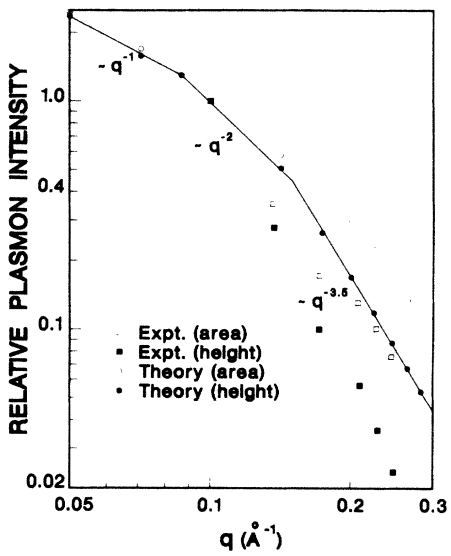

FIG. 8. Plasmon intensities are measured, and also calculated, by the peak height and the peak area, as shown in this figure. Note that the plotted intensities have been weighted by their corresponding plasmon intensity at $q=0.1$ Å^{-1}. The most interesting feature about the plasmon intensities found in our calculation is that the q dependence of the intensities varies as q varies, as is indicated in the figure. This feature is not confirmed by the measurement, possibly because of insufficient data in the $q<0.1$ Å^{-1} region. There also appears to be quite a large difference between the measured and the calculated intensities, but the discrepancy might be due to the inaccurate parameters employed in our calculation. More discussion on this point can be found in the main text.

In this section, we have shown that our theory quite successfully explains the quadratic q dependence of both the plasmon energy dispersion and the plasmon width. We have also found that damping basically explains the reported q^{-4} dependence of the plasmon peak intensity, but the region where this relation holds differs between our calculation and the measurement. We argued that the difference might be due to the inaccurate Fermi energy we used for our calculation—an argument that needs experimental justification. It was further suggested that careful measurements at small q could provide us with a valuable testing ground to examine our theory. Experimentally, attempts should also be made to increase the measurement resolution, so that the bipeak plasmon structure predicted by our theory could possibly be observed.

V. CONCLUDING REMARKS

In this paper, we have done a detailed calculation of the dielectric function for stage-1 GIC's, based on a superlattice model that contains an infinite array of graphite layers. Each graphite layer is described by the 2D model of Blinowski *et al.* The Coulomb interaction between layers is considered in our calculation, although interlayer tunneling is neglected. One major achievement of this work is that the calculation has been done nearly exactly and the results expressed analytically, so that the dielectric function could be easily employed in different calculations. One should be cautioned, however, that our dielectric function is calculated according to a linear-response theory, and there are calculations[14] showing that the nonlinear screening is important in graphite, especially when ε_F is small.

One application of the dielectric function is given in this paper in the form of a study of the plasmon structure of GIC's. Owing to the introduction of a layered superlattice, there exists a plasmon band in the excitation spectrum. Nevertheless, we have shown that plasmons are mainly three dimensional in behavior. By a close comparison with measurements, we have also shown that our theory could quantitatively explain the quadratic q dependence of both the plasmon energy and the plasmon width. However, the comparison of plasmon intensities has not been equally successful so far. On the one hand, we demonstrated that damping, due to the interband e-h excitations, causes the plasmon peak height to be proportional to $\sim q^{-4}$ at large q, which has been found experimentally. On the other hand, our calculated plasmon intensities seem too large compared with measurements. There are indications that the discrepancy might be due to inaccurate parameters used in our calculation, and this is because accurate measurements of these parameters are

not available. Obviously, more experimental investigation is needed, both to examine our theory and to accurately measure the parameters ε_F, ω_p^0, and ϵ_0.

The presence of a plasmon band also predicts bipeak plasmon structure in the electron energy-loss spectra. However, this bipeak structure is not observed experimentally, because of poor resolution in q. But by increasing the resolution by a factor of 10, we expect that this very distinctive plasmon structure will be measurable (see Fig. 5).

Generally speaking, our theory quite successfully explains the plasmon structure of the graphite system. This suggests that the superlattice model we used is a plausible one for GIC's. Some of the plasmon properties (e.g., the presence of a plasmon band) that we have obtained are quite general[7] in systems with superlattice structure (e.g., semiconductor superlattices). In recent years, there has been rapid progress in the study of semiconductor superlattices.[15–17] These studies should be helpful when we extend our theory of GIC's to include effects that have been neglected thus far, for example, surface effects.[16,17]

We have employed many approximate methods in our calculation; for example, we have neglected the interlayer tunneling, we have applied the RPA in our calculation, we have restricted the effects of intercalants to the determination of ε_F (and also of ϵ_0), etc. But in return, we have the advantage of applying a dielectric function which is expressed analytically and is independent of details of intercalants as long as ε_F is known. This not only means we could apply our theory to various stage-1 GIC's of different intercalants, but also means that the theory could be employed for other low-stage ($n \leq 4$) GIC's—since the band structure of low-stage GIC's is not very different for differing values of n.[3] We have tested our theory for stage-2 GIC's in the calculation of lifetime effects on the edge structure of optically induced interband transitions, and we have found satisfactory results there.[8] The relation between our dielectric function and low-stage GIC's is similar to that between Lindhard's dielectric function and simple metals, in the sense that in both cases the dielectric function only depends on the density of free charge carriers in the system (or equivalently, ε_F). Therefore, despite shortcomings relating to the approximations we have made, we expect our dielectric function—in much the same way as Lindhard's RPA result does for simple metals—to explain basic dielectric properties for low-state GIC's.

ACKNOWLEDGMENTS

The author thanks G. D. Mahan and B. Sernelius for stimulating and helpful discussions. He also thanks D. Meltzer for a critical reading of the manuscript. This research was sponsored jointly by the National Science Foundation through Grant No. DMR-85-01101, and by the Division of Materials Sciences, U.S. Department of Energy under Contract No. DE-AC05-84OR21400 with Martin Marietta Energy Systems, Inc.

APPENDIX A

In this appendix, we evaluate for the 2D model of GIC's the response functions $\chi^{a,b}(q,\omega)$ which were defined by Eq. (15) in the main text. In the process, an electron at the $\mathbf{k}$ state in the valence band is excited to the $\mathbf{k}'$ state ($\mathbf{k}'=\mathbf{k}+\mathbf{q}$). If the $\mathbf{k}'$ state is also in the valence band, it is an intraband transition described by $\chi^a(q,\omega)$; if the $\mathbf{k}'$ state is in the conduction band instead, it is an interband transition described by $\chi^b(q,\omega)$. The two cases are treated, respectively, in Secs. 1 and 2 of this appendix. In each case, an analytic expression for the imaginary part is derived first ($\chi^{a,b}=\chi_1^{a,b}+i\chi_2^{a,b}$), and the real part is subsequently found by means of the Kramers-Kronig relation

$$\chi_1^{a,b}(q,\omega)=\frac{-1}{\pi}\int_{-\infty}^{\infty}\chi_2^{a,b}(q,\omega')\mathrm{P}\left[\frac{1}{\omega-\omega'}\right]d\omega' . \tag{A1}$$

1. $\chi^a(q,\omega)$

It is more convenient to evaluate $\chi_2^a(q,\omega)$ in terms of hole states, i.e., considering that we annihilate a hole at the $\mathbf{k}$ state and meanwhile create a hole at the $\mathbf{k}'$ state. Noting that the hole at the $\mathbf{k}$ state has the energy $\varepsilon_k=v_f k$ and that holes occupy all the states with $k<k_f$, we can readily write down ($\mathbf{k}'=\mathbf{k}+\mathbf{q}$)

$$\chi_2^a(q,\omega)=\frac{-I^2(q)}{\pi}\times\int_0^{k_F}dk\,k\int_0^{\pi}d\psi\left[1+\frac{k+q\cos(\psi)}{k'}\right]\times\Theta(k'-k_F)\delta(\omega-v_f k'+v_f k) , \tag{A2}$$

where ψ is the angle between the initial state $\mathbf{k}$ and the momentum transfer $\mathbf{q}$. Note that the spin degeneracy and the existence of two identical valleys in the band structure have already been accounted for in this expression. Equation (A2) is actually only valid for $\omega>0$, but since $\chi_2^a(q,\omega)$ is antisymmetric under $\omega\rightarrow-\omega$ [i.e., $\chi_2^a(q,-\omega)=-\chi_2^a(q,\omega)$], it is sufficient to study Eq. (A2). After expressing $\mathbf{k}'$ in terms of $\mathbf{k}$, $\mathbf{q}$, and the angle ψ, the integration of this equation is elementary, although due attention should be paid to keep $k'>k_f$ and the angle ψ real (i.e., $|\cos\psi|\leq 1$). The result is ($\varepsilon_q=v_f q$)

$$\chi_2^a(q,\omega)=\frac{-q^2I^2(q)}{2\pi(\varepsilon_q^2-\omega^2)^{1/2}}[F(\omega)-F(-\omega)]\Theta(\varepsilon_q-|\omega|) , \tag{A3}$$

where

$$F(\omega)=\Theta(T(\omega)-1)\left[\frac{T(\omega)}{2}(T^2(\omega)-1)^{1/2}-\tfrac{1}{2}\ln[T(\omega)+(T^2(\omega)-1)^{1/2}]\right] \tag{A4}$$

and

$$T(\omega)=\frac{2\varepsilon_F+\omega}{\varepsilon_q} .$$

Since $\chi_2^a(q,\omega)$ in Eq. (A3) has already acquired a form that is valid for all ω, it can therefore be applied directly in Eq. (A1) to evaluate $\chi_1^a(q,\omega)$. Equivalently, we can evaluate

$$H^a(\omega)=\frac{-q^2I^2(q)}{2\pi^2}\int_{-\varepsilon_q}^{\varepsilon_q}d\omega'\frac{F(\omega')}{(\varepsilon_q^2-\omega'^2)^{1/2}}\frac{1}{\omega'+\omega} \tag{A5}$$

and get

$$\chi_1^a(q,\omega)=[H^a(\omega)+H^a(-\omega)]\ . \tag{A6}$$

But in practice, the complexity of $F(\omega)$ prevents us from calculating $H^a(\omega)$ exactly. In order to proceed, we expand $F(\omega)$ into a power series of (ω/ε_q), which is less than 1 according to Eq. (A3). In doing the expansion, we also made the assumption that $\varepsilon_q/2\varepsilon_F\le 1$, and found (denoting $2\varepsilon_F/\varepsilon_q$ by x and ω/ε_q by y)

$$F(y)=a+by+cy^2+dy^3+ey^4\ , \tag{A7}$$

where the coefficients $a,b,\ldots$ are functions of x. From symmetry considerations [see Eq. (A6)], we only need odd terms of Eq. (A7) to calculate $\chi_1^a(q,\omega)$, and we get

$$\chi_1^a(x,y)=\frac{\varepsilon_q I^2(q)}{2\pi v_f^2}\left[\frac{2\Theta(|y|-1)}{(y^2-1)^{1/2}}(b|y|+d|y|^3)-[2b+(2y^2+1)d]\right], \tag{A8}$$

where

$$b=x-\frac{1}{2}\frac{1}{x}+\frac{1}{8}\frac{1}{x^3},\quad d=-\frac{1}{6}\frac{1}{x^3}+\frac{1}{4}\frac{1}{x^5}\ .$$

This approximation is found to have an error within a few percent for $\varepsilon_q<2\varepsilon_F$ and produces responsible results [compared with the numerical calculation of Eq. (A5)], even if ε_q is slightly larger than $2\varepsilon_F$ (e.g., for $\varepsilon_q\sim 2.5\varepsilon_F$). Therefore, Eq. (A8), together with Eqs. (A3) and (A4), suits our needs for describing the low-energy intraband transitions, for which only small q is involved.

2. $\chi^b(q,\omega)$

Considerations similar to those which led to Eq. (A2) enable us to express

$$\chi_2^b(q,\omega)=\frac{-I^2(q)}{\pi}\int_0^{k_D}dk\,k\int_0^{\pi}d\psi\left[1-\frac{k+q\cos(\psi)}{k'}\right]\Theta(k'-k_f)\delta(\omega-v_fk'-v_fk)\ . \tag{A9}$$

The only change has been that the "k hole" is now in the conduction band, and consequently this hole has the energy $-v_fk$ and can be at any state in the conduction band. The cutoff k_D is an artificially determined quantity that measures the size of the conduction band. We could estimate this k_D by extending the region where $\varepsilon_k\propto|\mathbf{k}|$ and require that the number of states included match the number of the lattice sites; i.e., we demand that

$$2\times\frac{1}{2\pi}\int_0^{k_D}k\,dk=\frac{1}{A}\ , \tag{A10}$$

where A is equal to the area of a primitive cell. The factor of 2 here accounts for both U and U' points; hence, we get

$$\varepsilon_D=v_fk_D=2.33\gamma_0\approx 5.5\text{ eV}\ . \tag{A10'}$$

Since ε_D lies far outside of the range of energy transfer in which we are interested, the estimation of k_D is not expected to severely affect our results derived from it.

Without further approximation, the integration of Eq. (A9) could be executed straightforwardly, and the result is (for $\omega>0$)

$$\chi_2^b(q,\omega)=\frac{-I^2(q)}{4\pi}\frac{q^2}{(\omega^2-\varepsilon_q^2)^{1/2}}[\theta_c-\tfrac{1}{2}\sin(2\theta_c)]\times\Theta(\omega-\varepsilon_q)\Theta\left[1-\frac{2\varepsilon_F-\omega}{\varepsilon_q}\right]\Theta(2\varepsilon_D-\omega)\ , \tag{A11}$$

where

$$\theta_c=\begin{cases}\cos^{-1}\left[\dfrac{2\varepsilon_F-\omega}{\varepsilon_q}\right] & \text{if } \omega-2\varepsilon_F<\varepsilon_q \text{ (region I)}\ ,\\ \pi & \text{if } \omega-2\varepsilon_F>\varepsilon_q \text{ (region II)}\ .\end{cases} \tag{A11'}$$

To calculate the real part of $\chi_1^b(q,\omega)$, it is convenient to first evaluate

$$H^b(\omega)=\frac{1}{\pi}\int_0^{2\varepsilon_D}\chi_2^b(q,\omega')\mathrm{P}\left[\frac{1}{\omega'-\omega}\right]d\omega'\ , \tag{A12}$$

and then use the relation

$$\chi_1^b(q,\omega)=H^b(\omega)+H^b(-\omega)\ . \tag{A12'}$$

$H^b(\omega)$ has contributions from regions I and II [Eq. (A11')], i.e., $H^b(\omega)=H^{(\mathrm{I})}(\omega)+H^{(\mathrm{II})}(\omega)$. For $H^{(\mathrm{II})}(\omega)$ the integration is elementary and the result is

$$H^{(\mathrm{II})}(\omega)\frac{-I^2(q)}{4\pi}\frac{q}{v_f}F\left[\frac{\omega}{\varepsilon_q},\theta\right]\Bigg|_{\theta=\theta_1}^{\theta=\theta_2}\ , \tag{A13}$$

where

$$F(y,\theta)=\int\frac{d\theta}{1-y\cos(\theta)} \tag{A13'}$$

and the angles are $\theta_1=\cos^{-1}(\varepsilon_F/2\varepsilon_F+\varepsilon_q)$ and $\theta_2=\cos^{-1}(\varepsilon_q/2\varepsilon_D)$. The integration of Eq. (A13') can be done analytically; see, for example, Ref. 18. Thus, we have evaluated $H^{(\mathrm{II})}(\omega)$ exactly. In order to evaluate $H^{(\mathrm{I})}(\omega)$ we need to expand θ_c and $\sin(2\theta_c)$ of Eq. (A11) into a power series, but afterwards the integration is elementary. We found, with $y=\omega/\varepsilon_q$,

$$H^{(1)}=\frac{-I^2(q)}{4\pi^2}\frac{q}{v_f}\left[\left[b'+\frac{d'}{2}+d'y^2\right]\ln\left|\tan\left[\frac{\pi}{4}+\frac{\theta}{2}\right]\right|+\left[c'+\frac{d'}{2\cos(\theta)}\right]\tan(\theta)\right.$$
$$\left.+(a'+b'y+c'y^2+d'y^3)F(y,\theta)\right]\Bigg|_{\theta=\theta_3}^{\theta=\theta_4}, \tag{A14}$$

where the integration limits are determined by

$$\theta_3=\begin{cases}\cos^{-1}\left[\dfrac{\varepsilon_q}{2\varepsilon_F-\varepsilon_q}\right], & \text{if } \varepsilon_F>\varepsilon_q\\ 0, & \text{if } \varepsilon_F<\varepsilon_q\end{cases},$$
$$\theta_4=\cos^{-1}\left[\frac{\varepsilon_q}{2\varepsilon_F+\varepsilon_q}\right], \tag{A15}$$

and the coefficients have the following values ($x=2\varepsilon_F/\varepsilon_q$):

$$a'=\frac{\pi}{2}-2x+\tfrac{1}{3}x^3,\quad b'=2-x^2,\quad c'=x,\quad d'=-\tfrac{1}{3}. \tag{A16}$$

In Eq. (A14), terms that are an odd function of ω have been dropped because of Eq. (A12'). Using Eqs. (A11)—(A16), we have therefore determined $\chi^b(q,\omega)$, the response function due to interband transitions.

APPENDIX B

When we discussed the electron-energy-loss spectra in Sec. V, we made the approximation that the probing electron was described by a wave packet of zero width at the layer $l_0=0$. Relating to this approximation, two discussions are given in this appendix. In Sec. 1, the approximation that the wave packet is completely localized on a given layer is relaxed, and a finite width wave packet is considered. In Sec. 2, we analytically carry out the calculation of $\mathrm{Im}[-1/\varepsilon^s(q,\omega)]$ for the part due to electron-hole excitations. It should be noted that the application of this result is not restricted to the study of energy-loss spectra, but is also valid in cases when the perturbing potential is exerted from one of the graphite layers, e.g., in the study of deexcitations of conduction (or valence) electrons.[8]

1. Finite width wave packet

For a probing electron located on the layer l_0, the unscreened potential affecting the layer l, $v_l^{ex}(q,\omega)$, is simply $V_l(q)$ of Eq. (20)—as discussed in the main text. If instead, we approximate the probing electron by a wave packet of a finite size I_c and a uniform density distributed between $-I_c/2$ and $I_c/2$, we find a different potential

$$v_l^{ex}(q,\omega)=\frac{v_q}{I_c}\int_{|l|I_c+I_c/2}^{|l|I_c-I_c/2}e^{-|z|q}dz, \tag{B1}$$
$$=\begin{cases}\dfrac{2v_q}{qI_c}(1-e^{-qI_c/2}) & \text{if } l=l_0,\\ \dfrac{2v_q}{qI_c}e^{-|l|I_cq}\sinh\left[\dfrac{qI_c}{2}\right] & \text{if } l\neq l_0.\end{cases} \tag{B1'}$$

By applying the Fourier transformation according to Eq. (26), we get

$$v^{ex}(q,k_z,\omega)=\frac{2v_q}{qI_c}\sinh\left[\frac{qI_c}{2}\right]\left\{S(q,k_z)+\left[1-\cosh\left[\frac{qI_c}{2}\right]\right]\right\}. \tag{B2}$$

The k_z-independent second term above $[1-\cosh(qI_c/2)]$ could be neglected for small q, where the plasmon behavior is interesting. In this case, the correction due to the introduction of a finite-size wave packet is merely an extra factor of $[(2/qI)_c\sinh(qI_c/2)]$. This fact is very close to one in the small-q region. Therefore, $P(q,\omega)$ of Eq. (38) is a good description for the plasmon spectrum even when the probing electron has finite extension in space.

The expression in Eq. (B1) could be interpreted differently, so that $v_l^{ex}(q,\omega)$ is the averaged potential due to a narrow (compared with I_c) wave packet that passes through the layer l_0. This is a more realistic model than the previous one in describing the electron scattering experiment since, in fact, the "fast" probing electron does travel mostly in the interstices between graphite layers. The reason that we only took the potential average between $l_0-I_c/2$ and $l_0+I_c/2$ [see Eq. (B1)] follows from the fact that all graphite layers are identical to each other in an infinite system. Applying arguments similar to those following Eq. (B2), we can conclude that $P(q,\omega)$ of Eq. (38) is valid in this case as well.

We have considered two cases in which the probing electron is not confined to a given graphite layer: in the first, the electron has finite extension in space, and in the other, its movement is considered. In both cases, we found that Eq. (38) is a good description of the energy-loss spectra. One important assertion which follows from the discussions is that all plasmon modes in the plasmon band could be excited, and this finding is important in interpreting the spectra.

2. $\mathrm{Im}[-1/\epsilon^s(q,\omega)]$

The electron-hole contribution to $\mathrm{Im}[-1/\epsilon^s(q,\omega)]$, defined by Eq. (38), is calculated in this part. By putting $x=I_ck_z$, we can reformulate:

$$\mathrm{Im}\left[\frac{-1}{\epsilon^s(q,\omega)}\right]=A\int_0^{2\pi}\frac{dx}{\cos^2(x)+\beta\cos(x)+\gamma}, \tag{B3}$$

where $[\chi(q,\omega)=\chi^a(q,\omega)+\chi^b(q,\omega)=\chi_1(q,\omega)+i\chi_2(q,\omega)]$

$$A=\frac{v_q\chi_2(q,\omega)\sinh^2(qI_c)}{2\pi\epsilon_0^2}$$

and

$$\beta=-2\mu=-2\left[\cosh(qI_c)+\frac{v_q\chi_1(q,\omega)}{\epsilon_0}\sinh(qI_c)\right],$$
$$\gamma=\mu^2+\nu^2,\quad \nu=\frac{v_q\chi_2(q,\omega)}{\epsilon_0}\sinh(qI_c)\ . \tag{B4}$$

The integration in Eq. (B3) can be performed exactly. First, let us rewrite:

$$\mathrm{Im}\left[\frac{-1}{\epsilon^s(q,\omega)}\right]=\frac{A}{2i\nu}\int_0^{2\pi}dx\left[\frac{1}{\cos(x)+s}-\frac{1}{\cos(x)+s^*}\right], \tag{B5}$$

where

$$s=\tfrac{1}{2}(\beta-2i\nu)\ . \tag{B5'}$$

Since s is complex, it is easier to perform the integration in the complex z plane, i.e., evaluate a contour integral along the unit circle. With the change of variable, $z=e^{ix}$, the denominator of each of the two integrands is quadratic in z and hence has two roots. The roots of the first integrand in Eq. (B5) are

$$z_\pm=s\pm(s^2-1)^{1/2}\ , \tag{B6}$$

and those of the second integrand are $z_\pm^*$. It is easy to show from the discussion above that

$$\mathrm{Im}\left[\frac{-1}{\epsilon^s(q,\omega)}\right]=\frac{A\pi}{i\nu}\left[\frac{1}{(s^2-1)^{1/2}}-\frac{1}{(s^{*2}-1)^{1/2}}\right]$$
$$\times[\Theta(1-|z_+|)-\Theta(1-|z_-|)]\ . \tag{B7}$$

The presence of the step functions above are due to the fact that only the root (or roots) enclosed by the unit circle contributes to the integration. Since $|z_+|\,|z_-|=1$, only one of those step functions is nonvanishing. We found that $|z_+|>1$, hence the step functions in Eq. (B7) could be simply replaced by the factor -1. With a few more steps of elementary algebra, we can express Eq. (B7) by the following formalism, which readily shows $\mathrm{Im}[-1/\epsilon^s(q,\omega)]$ to be both real and positive: i.e.,

$$\mathrm{Im}\left[\frac{-1}{\epsilon^s(q,\omega)}\right]=\frac{2\pi A}{\nu|s^2-1|}\left[\frac{|s^2-1|-\mu^2+\nu^2+1}{2}\right]^{1/2}, \tag{B8}$$

where

$$|s^2-1|=[(\gamma-1)^2+4\nu^2]^{1/2}\ .$$

This last expression, together with Eq. (B4), could be easily employed in the calculation of the electron-energy-loss spectra. By using the relation $\gamma\gg\mu\sim\nu\gg1$ in the weak-coupling limit (i.e., $qI_c\gg1$), one can show easily that Eq. (B8) reduces to the 2D expression $\mathrm{Im}[-1/\epsilon^{2D}(q,\omega)]$—as may have been expected.

[1] M. S. Dresselhaus and G. Dresselhaus, Adv. Phys. **30**, 139 (1981).
[2] J. J. Ritsko and M. J. Rice, Phys. Rev. Lett. **42**, 666 (1979).
[3] J. Blinowski, Nguyen Hy Hau, C. Rigaux, J. P. Vieren, R. le Toullee, G. Furdin, A. Herold, and J. Melin, J. Phys. (Paris) **41**, 47 (1980); J. Blinowski and C. Rigaux, *ibid.* **41**, 667 (1980).
[4] J. C. Slonczewski and P. R. Weiss, Phys. Rev. **109**, 272 (1958).
[5] D. M. Hoffman, R. E. Heinz, G. L. Doll, and P. C. Eklund, Phys. Rev. B **32**, 1278 (1985).
[6] H. Ehrenreich and M. H. Cohen, Phys. Rev. **115**, 786 (1959).
[7] S. Das Sarma and J. J. Quinn, Phys. Rev. B **25**, 7603 (1982).
[8] K. W.-K. Shung, Phys. Rev. B (to be published).
[9] C. Zener, Phys. Rev. **36**, 51 (1930).
[10] D. Pines and P. Nozières, *The Theory of Quantum Liquids* (Benjamin, New York, 1966).
[11] A. Fetter, Ann. Phys. **81**, 367 (1973); *ibid.* **88**, 1 (1974).
[12] E. J. Mele and J. J. Ritsko, Solid State Commun. **33**, 937 (1980).
[13] E. A. Taft and H. R. Philipp, Phys. Rev. **138**, A197 (1965). Our ϵ_0 corresponds to $(1+\delta\epsilon_1^\sigma)$ in this reference. From Fig. 3 therein, one finds that $\delta\epsilon_1^\sigma$ can be approximated by 1.4 if the energy is less than 5 eV.
[14] D. P. DiVincenzo and E. J. Mele, Phys. Rev. B **29**, 1685 (1984).
[15] A. C. Tselis and J. J. Quinn, Phys. Rev. B **29**, 3318 (1984).
[16] P. Hawrylak, J.-W. Wu, and J. J. Quinn, Phys. Rev. B **32**, 4272 (1985); **32**, 5169 (1985).
[17] J. K. Jain and P. B. Allen, Phys. Rev. Lett. **54**, 947 (1985).
[18] I. S. Gradshteyn and I. M. Ryzhik, *Table of Integrals, Series, and Products* (Academic, New York, 1980).